catalysts

MDPI

Article

Efficient N, Fe Co-Doped TiO_2 Active under Cost-Effective Visible LED Light: From Powders to Films

Sigrid Douven [1,*], Julien G. Mahy [1,2], Cédric Wolfs [1], Charles Reyserhove [1], Dirk Poelman [3], François Devred [2], Eric M. Gaigneaux [2] and Stéphanie D. Lambert [1]

1 Department of Chemical Engineering—Nanomaterials, Catalysis & Electrochemistry, University of Liège, B6a, Quartier Agora, Allée du six Août 11, 4000 Liège, Belgium; julien.mahy@uclouvain.be (J.G.M.); cedric.wolfs@uliege.be (C.W.); charles.reyserhove@gmail.com (C.R.); stephanie.lambert@uliege.be (S.D.L.)

2 Institute of Condensed Matter and Nanosciences—Molecular Chemistry, Materials and Catalysis (IMCN/MOST), Université catholique de Louvain, Place Louis Pasteur 1, Box L4.01.09, 1348 Louvain-La-Neuve, Belgium; francois.devred@uclouvain.be (F.D.); eric.gaigneaux@uclouvain.be (E.M.G.)

3 LumiLab, Department of Solid State Sciences, Ghent University, 9000 Gent, Belgium; dirk.poelman@ugent.be

* Correspondence: S.Douven@uliege.be; Tel.: +32-4-366-3563

Received: 6 April 2020; Accepted: 8 May 2020; Published: 14 May 2020

Abstract: An eco-friendly photocatalytic coating, active under a cost-effective near-visible LED system, was synthesized without any calcination step for the removal of organic pollutants. Three types of doping (Fe, N and Fe + N), with different dopant/Ti molar ratios, were investigated and compared with undoped TiO_2 and the commercial P25 photocatalyst. Nano-crystalline anatase-brookite particles were successfully produced with the aqueous sol-gel process, also at a larger scale. All samples displayed a higher visible absorption and specific surface area than P25. Photoactivity of the catalyst powders was evaluated through the degradation of *p*-nitrophenol in water under visible light (>400 nm). As intended, all samples were more performant than P25. The N-doping, the Fe-doping and their combination promoted the activity under visible light. Films, coated on three different substrates, were then compared. Finally, the photoactivity of a film, produced from the optimal N-Fe co-doped colloid, was evaluated on the degradation of (i) *p*-nitrophenol under UV-A light (365 nm) and (ii) rhodamine B under LED visible light (395 nm), and compared to undoped TiO_2 film. The higher enhancement is obtained under the longer wavelength (395 nm). The possibility of producing photocatalytic films without any calcination step and active under low-energy LED light constitutes a step forward for an industrial development.

Keywords: photocatalysis; Fe/N doping; titania; aqueous sol-gel process; LED visible light

1. Introduction

The last centuries have seen a steady increase in human activities, causing a remarkable technological development and soaring human populations. However, the industrial expansion has brought atmospheric, ground and water pollution, all harmful for humans and the environment [1]. Indeed, major pollution can cause human diseases like breathing problems, cardiovascular problems, cancers, neurobehavioral disorders, etc. It can also affect global warming, which worsens climate change, increases sea level rises and causes serious damage on e.g., animals and flora [1]. Major anthropogenic pollutants are aromatic compounds, pesticides, chlorinated compounds, SO_x, NO_x, heavy metals or petroleum hydrocarbons [1]. In order to decrease this emitted pollution, various chemical, physical and biological treatments exist [2,3]. Some molecules (like micropollutants and

pharmaceuticals) are not eliminated or degraded by these processes and additional specific treatments are required to remove this small residual fraction of pollution. Among the possible methods, photocatalysis is a technique well-developed in the past years [4].

This technique consists of a set of redox reactions between organic pollutants and radicals or other active species. A semiconductor photocatalyst and any UV light source are required since the first active species are generated by the illumination of the photocatalyst [5,6]. This mechanism promotes the production of highly reactive species able to react and decompose organic molecules. In the best case, the final decomposition products are CO_2 and H_2O [5,6].

The most common photocatalyst is titanium dioxide (TiO_2) under the anatase phase [7–9]. The amount of energy required to activate anatase TiO_2 is high. Indeed, the width of its band gap (3.2 eV) corresponds to a light source with a wavelength inferior or equal to 388 nm [10]. This wavelength corresponds to UV radiation, which is more energetic than visible light.

The conventional light sources used for photocatalytic processes have several disadvantages like a high energy consumption, a high operational temperature (600–900 °C), difficulty in operation, and a short life span of between 500 and 2000 h [11–13]. In recent years [13–17], research has focused on the development of alternative lighting systems for photocatalytic water treatment using light-emitting diodes (LED). This lighting presents several advantages: it is cost-effective, eco-friendly, compact, with a narrow spectrum and a very long life span (> 50,000 h) [13–17]. However, UV LEDs have low efficiencies, with e.g., [18] taking pride in 20% external quantum efficiency for a 275-nm monochromatic LED. Decreasing the band gap of the photocatalyst, i.e., shifting toward visible LED, is thus very effective regarding the energy consumption.

The use of TiO_2 as photocatalyst has two main limitations [10]: (i) the fast charge recombination and (ii) the large band gap value. Indeed, if the recombination of the photo-generated species (e^- and h^+) is fast, the production of radicals is low and the degradation is less effective. Furthermore, as explained above, if the band gap is large, the energy required for the electron transfer is high and only UV radiation can be used.

To prevent these limitations, several studies have been carried out. Regarding the improvement of the recombination time, the major modification of TiO_2 materials is the addition of metallic nanoparticles or metallic ions as Ag [19,20], Au [19,21], Pt [22,23], Pd [20], Fe^{3+} [24–27] or Cu^{2+} [24,25,28]. In this case, the metallic nanoparticle or metallic ion plays a role of electron trap allowing to increase the recombination time [29]. Combination with other semiconductors has also been investigated [10] such as TiO_2/ZnO [30], TiO_2/CdS, TiO_2/Bi_2S_3 [10] or TiO_2/ZrO_2 [31]. In this case, synergetic effects lead to a better charge separation or an increased photostability. In order to extend the activity under visible light and therefore reduce the band gap, TiO_2 materials have been modified with different elements or molecules: (i) metallic ions [25,28,32] such as Cu [33] or Fe [26], (ii) dye molecules such as porphyrins [34–36] or (iii) non-metallic elements such as N [37–39], P [40,41], S [10,42] or F [10,43].

Depending on the application requirements, TiO_2 can be used as a powder or a film. Typically, the as-synthesized material is amorphous and has no photoactivity; it is subsequently calcined to increase its crystallinity and so, the photoactivity. For practical applications in water treatment, photocatalytic coatings are more convenient. Unlike powders, they do not require any filtration step. Nevertheless, increasing the amount of photocatalyst implies increasing the area of the coated surface, while it simply implies a higher concentration in the case of powders. In terms of design, increasing the coated surface is a challenging topic if one wants to fulfill space constraints and maximize illumination. Furthermore, calcination may be detrimental to the substrate. For example, stainless steel loses its anticorrosive properties after a high temperature treatment.

This study aims to develop an eco-friendly and efficient photocatalytic coating, active under a cost-effective near-visible LED system for the removal of organic pollutants. To reach this goal, the research was conducted in two steps: (i) crystalline TiO_2-based photocatalysts powders were prepared without any calcination step by a sol-gel process in water and the composition was optimized to extend photoactivity toward the visible range, then (ii) the best materials were coated on three

different substrates (bare and brushed stainless steel and glass substrates) to assess its efficiency on organic pollutants removal under a near-visible LED light source.

TiO_2 was co-doped with Fe and N in order to extend its activity toward the visible region and reduce the charge recombination. Different amounts of Fe and N were tested. The corresponding pure and single-doped catalysts were also synthesized. The powder materials were characterized by nitrogen adsorption–desorption, X-ray diffraction, inductively coupled plasma–optical emission spectroscopy, diffuse reflectance and X-ray photo-electron spectroscopy. The photocatalytic activity of the powder samples was evaluated through the degradation of *p*-nitrophenol (PNP, $C_6H_5NO_3$) under conventional halogen visible light ($\lambda > 400$ nm). The degradation experiments highlighted the influence of the dopants on the visible activity. The optimized materials were deposited on bare and brushed stainless steel and glass substrates. The photoactivity of those samples were assessed on the basis of the degradation of (i) PNP under UV-A light (365 nm) and (ii) rhodamine B under near-visible LED light (395 nm). The degradation efficiency was compared to the one obtained with pure TiO_2 coatings. In order to demonstrate the feasibility of an industrial development, one of our photocatalysts was synthesized in a pilot-scale equipment of 10 L and compared to the corresponding material obtained at laboratory scale.

2. Results and Discussion

2.1. Sample Crystallographic Properties

The X-ray diffraction patterns (XRD) of pure and three doped TiO_2 catalysts are presented in Figure 1. Similar XRD patterns were obtained for the other samples.

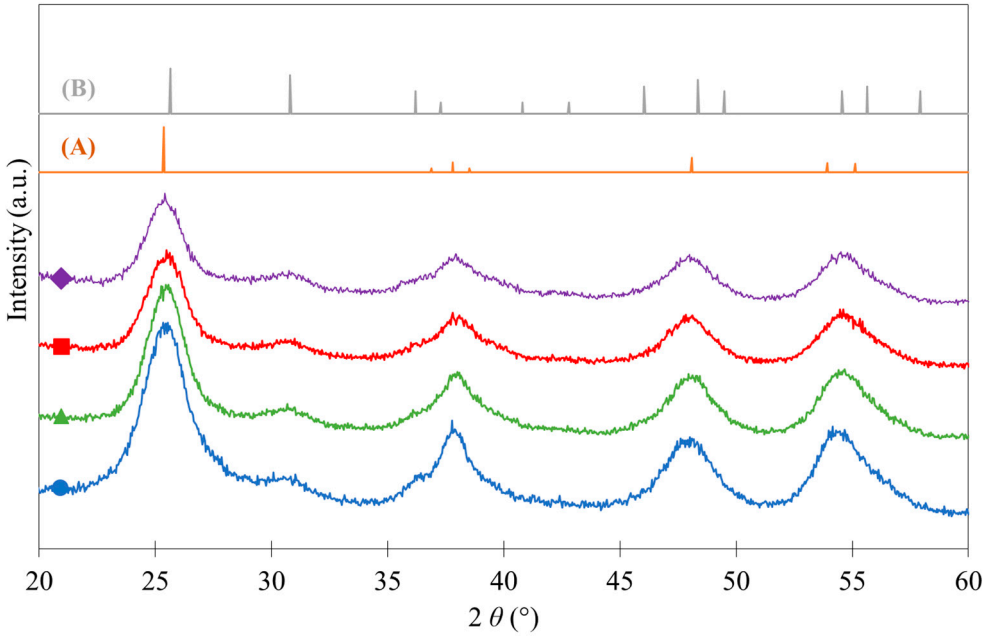

Figure 1. X-ray diffraction (XRD) patterns: (●) pure TiO_2, (▲) TiO_2/Fe0.5, (■) TiO_2/N43 and (♦) TiO_2/Fe0.5/N43. (A) Reference pattern of anatase and (B) reference pattern of brookite. Sample names and compositions are listed in Table 1.

Table 1. Textural and optical properties of TiO_2-based photocatalysts.

Sample	Fe Content mol/mol%	d_{XRD} nm ± 1	S_{BET} $m^2\ g^{-1}$ ± 5	V_{DR} $cm^3\ g^{-1}$ ± 0.01	V_p $cm^3\ g^{-1}$ ± 0.01	d_{BET} nm ± 1	$E_{g,direct}$ eV ± 0.01	$E_{g,indirect}$ eV ± 0.01
P25	– [1]	18[2]–8[3]	47	0.03	– [1]	31	3.45	3.05
Pure TiO_2	– [1]	5	180	0.09	0.10	9	3.25	2.90
TiO_2/Fe0.25	0.32	4	195	0.10	0.10	8	3.25	2.80
TiO_2/Fe0.5	0.56	5	180	0.10	0.10	9	3.20	2.75
TiO_2/N10	– [1]	5	185	0.10	0.10	8	3.15	2.90
TiO_2/N30	– [1]	4	185	0.09	0.09	8	3.15	2.90
TiO_2/N43	– [1]	5	220	0.11	0.11	7	3.20	2.90
TiO_2/N75	– [1]	4	210	0.11	0.11	7	3.20	2.90
TiO_2/Fe0.25/N10	0.28	4	155	0.08	0.08	10	3.10	2.80
TiO_2/Fe0.25/N30	0.27	4	200	0.10	0.10	8	3.10	2.75
TiO_2/Fe0.25/N43	0.27	4	240	0.12	0.12	6	3.10	2.80
TiO_2/Fe0.25/N75	0.31	4	235	0.12	0.12	7	3.15	2.70
TiO_2/Fe0.5/N10	0.54	5	185	0.10	0.10	8	3.05	2.70
TiO_2/Fe0.5/N30	0.54	4	210	0.11	0.11	7	3.1	2.65
TiO_2/Fe0.5/N43	0.55	4	230	0.12	0.12	7	3.05	2.65
TiO_2/Fe0.5/N75	0.53	4	220	0.11	0.11	7	3.05	2.65

[1] Not measured; [2] measured from anatase peak; [3] measured from rutile peak; S_{BET}: specific surface area estimated by the BET theory; V_{DR}: specific micropore volume estimated by the Dubinin–Raduskevitch method; d_{BET}: mean diameter of TiO_2 nanoparticles calculated from S_{BET} values; d_{XRD}: mean diameter of TiO_2 crystallites calculated using the Scherrer equation; $E_{g,direct}$: direct optical band gap values estimated with the transformed Kubelka–Munk function; $E_{g,indirect}$: indirect optical band gap values estimated with the transformed Kubelka–Munk function.

All samples are mainly composed of anatase with a small amount of brookite. The crystallite size, d_{XRD}, determined by the Scherrer equation (Equation (12) in Section 3.4) is 4–5 nm (Table 1) regardless of the nature or content of the dopant [33]. The calculated crystallite size could be slightly underestimated because of the presence of a small amount of brookite. The phase quantification is presented in Table 2. For all samples, the distribution between anatase and brookite phases was quite similar with ~90% of anatase and ~10% of brookite.

Table 2. Semi-quantitative analysis of sample crystallinity.

Sample	Anatase Content %	Brookite Content %	Rutile Content %
P25	80	–	20
Pure TiO_2	89	11	–
TiO_2/Fe0.25	90	10	–
TiO_2/Fe0.5	90	10	–
TiO_2/N10	91	9	–
TiO_2/N30	89	11	–
TiO_2/N43	91	9	–
TiO_2/N75	90	10	–
TiO_2/Fe0.25/N10	90	10	–
TiO_2/Fe0.25/N30	88	12	–
TiO_2/Fe0.25/N43	91	10	–
TiO_2/Fe0.25/N75	89	11	–
TiO_2/Fe0.5/N10	88	12	–
TiO_2/Fe0.5/N30	89	11	–
TiO_2/Fe0.5/N43	90	10	–
TiO_2/Fe0.5/N75	92	8	–

2.2. Textural Properties and Morphology

The nitrogen adsorption–desorption isotherms are presented in Figure 2 for four samples: pure TiO_2, TiO_2/Fe0.5, TiO_2/N43 and TiO_2/Fe0.5/N43. All other isotherms have a similar shape with a steep increase of the adsorbed volume at low pressure followed by a plateau. This corresponds to a microporous solid from the BDDT classification (type I isotherm) [44]. The corresponding specific surface area, S_{BET}, total pore volume, V_p, and micropore volume, V_{DR}, are reported in Table 1. The specific surface area varies between 155 and 240 $m^2\ g^{-1}$, while the total pore volume varies between 0.08 and 0.12 $cm^3\ g^{-1}$. The samples are essentially microporous, as the total pore volume is identical to the micropore volume. These surface properties are consistent with the ones usually found in literature for samples prepared with this peptization–precipitation method [33,45].

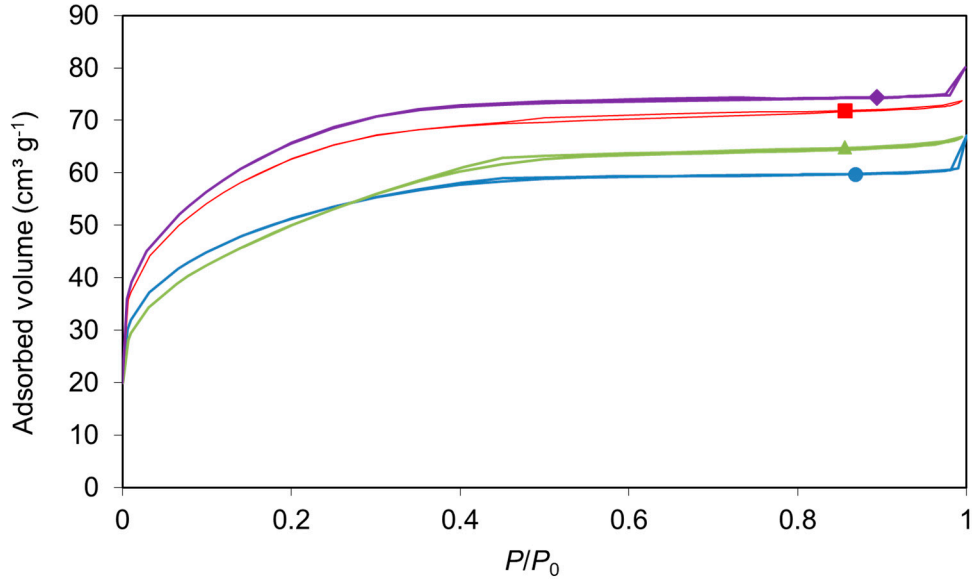

Figure 2. Nitrogen adsorption–desorption isotherms: (●) pure TiO_2, (▲) TiO_2/Fe0.5, (■) TiO_2/N43 and (♦) TiO_2/Fe0.5/N43.

A model developed earlier assumes that these materials are composed of spherical, non-porous TiO_2 nanoparticles between which small voids exist (i.e., < 2 nm, micropores) [26,33]. Thus, a particle size, d_{BET}, can be estimated from the S_{BET} value and Equation (11) (see Section 3.4). The values are reported in Table 1. For all samples, the d_{BET} is around 7–8 nm. The values are consistent with the ones determined by XRD and are independent of the nature and content of the dopant. Therefore, the assumption made before is realistic, and each spherical nanoparticle would correspond to one crystallite. This morphology is confirmed by transmission electron microscopy (TEM) observations from Figure 3 (see below).

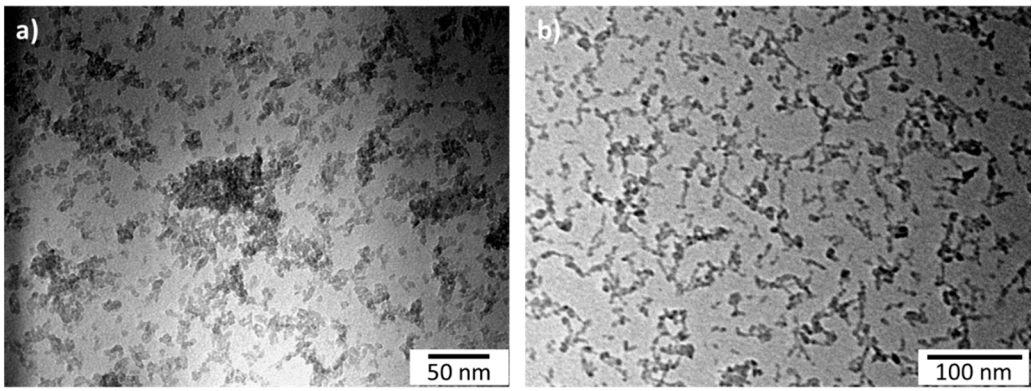

Figure 3. Transmission electron microscopy (TEM) pictures of (**a**) pure TiO_2 and (**b**) TiO_2/Fe0.5.

The isotherm of Evonik P25 (Figure S1 in Supplementary Materials) typically corresponds to a macroporous solid. At high pressure, the adsorbed volume increases asymptotically like in type II isotherm (macroporous solid) [44]. The S_{BET} and V_{DR} values are lower than pure and doped TiO_2 samples ones with values of 47 m^2 g^{-1} and 0.03 cm^3 g^{-1} respectively.

The morphology of the samples was visualized with a transmission electron microscope. The same morphology was observed for all samples with aggregates of spherical nanoparticles. The diameter of the nanoparticles is in the range of 5 to 8 nm. This size was similar to the crystallite size measured by XRD (Table 1). Pure TiO_2 and TiO_2/Fe0.5 TEM micrographs are presented in Figure 3 as examples.

2.3. Optical Properties

Optical properties were evaluated by diffuse reflectance spectroscopy. Figure 4 presents the evolution of the normalized Kubelka–Munk function F(R∞) with wavelength, λ, for the pure TiO_2, TiO_2/Fe0.5, TiO_2/N43, TiO_2/Fe0.5/N43 and Evonik P25.

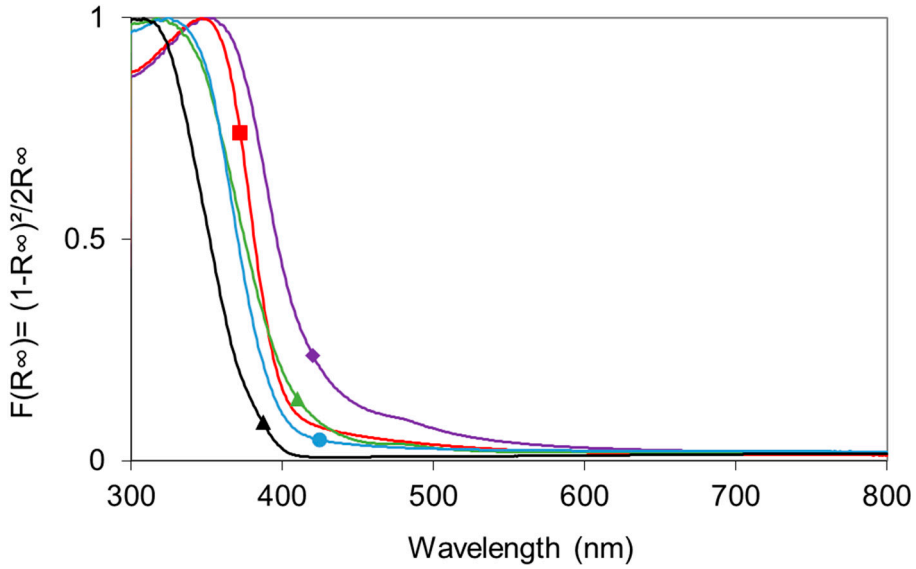

Figure 4. Normalized Kubelka–Munk function F(R∞) calculated from DR-UV-Vis absorbance spectra and transformed via the Kubelka–Munk function for (●) pure TiO_2, (▲) TiO_2/Fe0.5, (■) TiO_2/N43, (♦) TiO_2/Fe0.5/N43 and (▲) Evonik P25.

There is a clear shift of the curves towards longer wavelengths for all samples compared to Evonik P25, suggesting an activation under UV-Visible light. This result is in accordance with similar photocatalysts produced by different methods such as hydrothermal methods [46], sonochemical methods [47], and sol-gel methods in alcohol requiring calcination [48]. The pure TiO_2 is already shifted toward the visible compared to P25. This is probably due to nitrogen insertion during the synthesis [39]. Nitric acid is used as peptizing agent in the aqueous synthesis, leading to nitrogen insertion. The N-doping is confirmed by the XPS measurements (see Section 2.4). Adding iron to pure TiO_2 modifies the slope of the pure TiO_2 curve while adding nitrogen shifts it. The co-doped sample combines both effects (slope + translation) with, as a result, a higher shift than the single-doped samples.

The transformed Kulbelka–Munk function $(F(R\infty)h\nu)^{1/m}$ as a function of the energy enables to estimate the direct and indirect band gap values, taking m equal to $\frac{1}{2}$ and 2 respectively. The values are reported in Table 1. Both $E_{g,direct}$ and $E_{g,indirect}$ decrease with doping, suggesting a positive effect of iron and nitrogen on the activation under UV-Visible.

2.4. Sample Composition

The actual iron content, determined by inductively coupled plasma–optical emission spectroscopy (ICP-OES), is consistent with the intended content of iron introduced during the synthesis of the doped samples (Table 1).

The survey X-ray photo-electron spectroscopy (XPS) spectrum for the pure TiO_2 sample is presented in Figure S2 (Supplementary Materials). The different peaks (carbon, oxygen, nitrogen, titanium) are labelled. Similar spectra were obtained for all other samples. The intensity of the peaks representative of nitrogen is too low to make them visible on the general spectrum. Iron is not detected by XPS. This is probably due to the small amount and homogeneous distribution of iron in the sample. This has already been observed in literature [49].

Spectra specific to Ti *2p*, O *1s*, N *1s* and C *1s* are presented in Figure 5 for the TiO_2/Fe0.5/N43 sample.

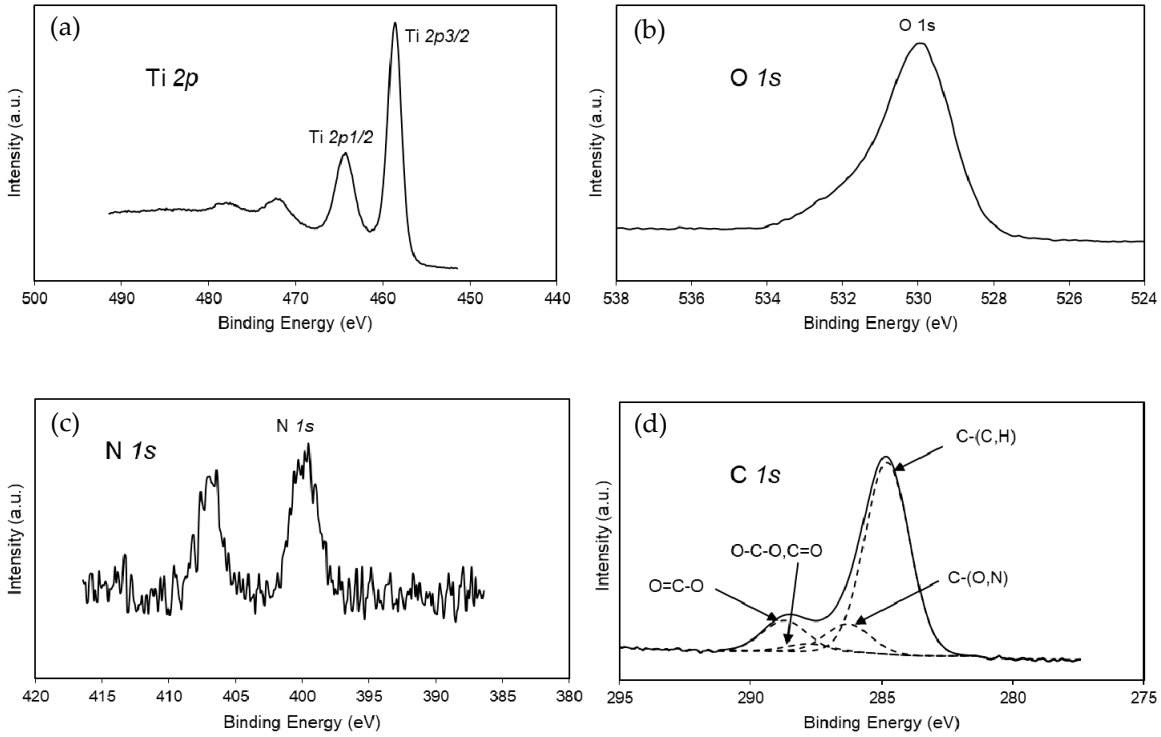

Figure 5. X-ray photo-electron spectroscopy (XPS) spectra of the TiO_2/Fe0.5/N43 sample: (**a**) Ti *2p* region, (**b**) O *1s* region, (**c**) N *1s* region and (**d**) C *1s* region.

The Ti *2p* spectrum (Figure 5a) shows the Ti *2p1/2* and Ti *2p3/2* peaks at 464 and 459 eV respectively. They are attributed to Ti^{4+} species in TiO_2 [39,50].

As for the O *1s* spectrum (Figure 5b), the sample's peak at 530 eV is associated to Ti–O in TiO_2. The tail at higher binding energy in the O *1s* peak is difficult to exploit because of the presence of a significant amount of oxygen caused by carbonaceous contamination accumulating at the surface of the sample (inherent to XPS and unavoidable) or bonded to nitrogen. The O *1s*/Ti *2p* ratio is around 2.5 which is close to the stoichiometric ratio in TiO_2. The gap between 2 and 2.5 is due to this oxygen involved in the surface carbonaceous contamination.

The C *1s* contribution is divided into four components (Figure 5d). The C–(C,H) contribution at 284.8 eV is a classical aliphatic carbon contamination used to calibrate the measurements. In our standard routine procedure for decomposing the C *1s* contribution, we define the contribution of carbon involved in simple bond with O or N at 1.5 eV higher (286.3 eV). The signals at a binding energy of around 288 eV are attributed to the contribution of C multiple-bonded to O. The other samples show comparable decomposition of the C signal.

In the case of the N *1s* spectrum (Figure 5c), two peaks are visible for pure TiO_2: one centered on 400 eV and one around 407 eV. According to literature, a N *1s* peak around 400 eV may correspond to interstitial Ti–O–N [50,51] leading to visible absorption. This activation under UV/Visible light is consistent with the diffuse reflectance measurements (Figure 4). Indeed, a higher visible absorption is observed in N-doped samples compared to Evonik P25. Other impurities such as ammonium ions also show an XPS peak at about 400 eV [52]. Since ammonium chloride was used for the N doping, the presence of NH_{4^+} could lead to a misleading interpretation of XPS results. This is the reason why samples were washed several times. The second peak at 407 eV may be linked to residual nitrate due to the residual nitric acid from the synthesis as shown in [39].

The two peaks related to nitrogen are present in all XPS spectra but there is no clear difference between the samples and the N/Ti ratios are quite similar for all samples. This has already been observed in the literature [53,54]. Even if increasing the amount of nitrogen during the synthesis does not seem to have an impact on the surface composition of the samples (XPS), all samples are actually different, as shown by diffuse reflectance tests (Section 2.3) and photocatalytic activity tests (Section 2.5). One possible explanation is the inhomogeneous repartition of nitrogen along the depth of the samples. Furthermore, even if the presence of photoactive N dopant is revealed by other techniques (optical absorption, Electron Paramagnetic Resonance), the signal sometimes seems to escape XPS detection, as pointed out by [52]. In Smirniotis et al. [53], the relative atomic concentrations of N in N-doped TiO_2 (aerosol synthesis) do not vary significantly between samples obtained with different concentration of nitric acid. Furthermore, the relative atomic concentrations obtained by XPS differ from the ones obtained by energy-dispersive X-ray (EDX) spectroscopy. In Gil et al. [54], nitrogen is not detected.

Let us mention that the small changes in the XRD patterns and in the N-signal in XPS show that the amount of nitrogen that is actually incorporated in the TiO_2 lattice is probably small, and clearly lower than 10 to 75%. So, in the label of the samples, the N content corresponds to the starting one.

2.5. Photocatalytic Activity of the Powders

Adsorption tests performed in the dark showed a mean adsorption of PNP of 3%. Results of the degradation tests are presented in Figure 6 for all samples. All samples have a better activity under visible light than P25 (~12% of PNP degradation), even for the pure TiO_2 (~25% of PNP degradation). As previously explained, due to the synthesis method and the use of nitric acid, all the samples are doped with nitrogen, even the pure TiO_2 sample. The best sample, TiO_2/Fe0.5/N43, reaches a PNP degradation of 67%.

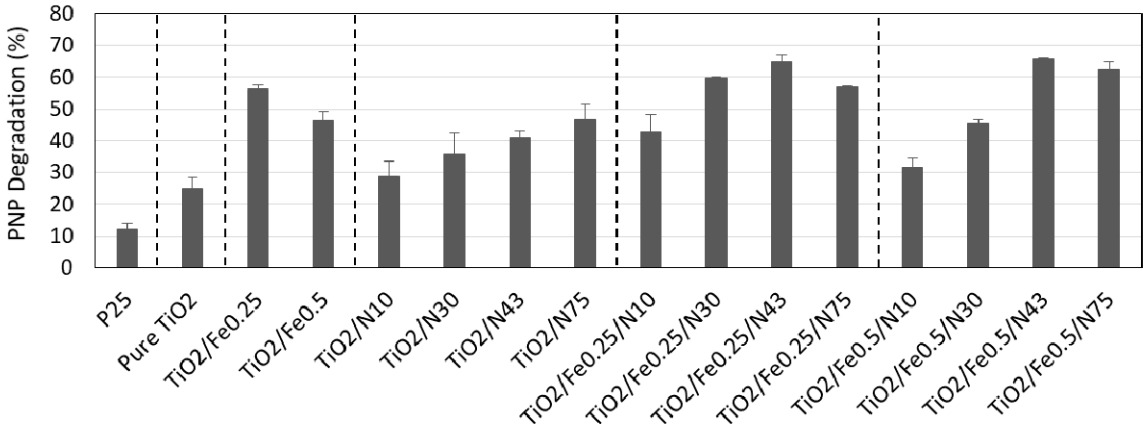

Figure 6. *p*-Nitrophenol (PNP) degradation (%) under visible light (λ > 400 nm) for all samples after 24 h of reaction time.

Both dopants have a positive effect on the degradation of PNP under the conditions of the catalytic experiments. For Fe single-doped TiO_2, 0.25 mol% of Fe enhances the photocatalytic activity, but increasing its content beyond that value becomes detrimental to the degradation of PNP [26].

During the peptization, the metal ion dopant species (M^{n+}) are hydrolyzed, leading to the formation of $[M_x(OH)_y]^{(nx-y)+}$. Hydroxylated species associated to Fe^{3+} dopant are known to be particularly stable, therefore increasing the –OH density at the surface of the catalyst [26]. This could explain the enhancement of the photocatalytic activity of the Fe^{3+}-doped samples owing to a higher production of hydroxyl radicals and a higher hydrophilicity. Furthermore, the reduction of the band gap value for Fe-doped samples (Table 1) suggests the presence of an intra-band gap level, thus reducing the energy required to activate the samples, i.e., shifting the activity toward visible.

The mechanism of organic pollutant degradation by pure TiO_2 is well-established [55]. By absorbing the energy brought by the light, free electrons (e^-) and holes (h^+) are generated and can react with O_2 and H_2O respectively to generate the corresponding oxidative species $O_2^{-\bullet}$ and $^\bullet OH$.

The use of Fe^{3+} induces the photo-Fenton effect, i.e. the photo-reduction of ferric ions into ferrous ones by reacting with water in the presence of light:

$$Fe^{3+} + H_2O + h\nu \rightarrow Fe^{2+} + {}^\bullet OH + H^+ \quad (1)$$

where h is the Planck constant (6.63×10^{-34} J.s) and ν is the light frequency (Hz).

There is therefore an increased production of hydroxyl radicals $^\bullet OH$ which can degrade organic pollutants.

Furthermore, Fe^{3+} can act as charge trapping sites, hindering the e^--h^+ recombination process. The photo-generated holes and electrons trapped by Fe^{3+} can easily be transferred to surface –OH groups and adsorbed oxygen at the surface of TiO_2 to produce $^\bullet OH$ and O_2^- radicals (see Equations (2) to (8)) [25,28,33]. This induces an enhanced photocatalytic activity.

$$Fe^{3+} + h^+ \rightarrow Fe^{4+} \quad (2)$$

$$Fe^{3+} + e^- \rightarrow Fe^{2+} \quad (3)$$

$$Fe^{2+} + O_2(ads) \rightarrow Fe^{3+} + O_2^- \quad (4)$$

$$Fe^{2+} + Ti^{4+} \rightarrow Fe^{3+} + Ti^{3+} \quad (5)$$

$$Ti^{3+} + O_2(ads) \rightarrow Ti^{4+} + O_2^- \quad (6)$$

$$Fe^{4+} + e^- \rightarrow Fe^{3+} \quad (7)$$

$$Fe^{4+} + OH^- (ads) \rightarrow Fe^{3+} + {}^\bullet OH(ads) \quad (8)$$

However, a high Fe^{3+} concentration is detrimental to the photocatalytic activity because Fe^{3+} acts as e^--h^+ recombination center through cyclic redox reactions without the generation of active radicals available for the photocatalytic degradation process.

Adding N to TiO_2 has a positive effect on the degradation of PNP. The higher the amount of N, the higher the degradation of PNP. The molar percentages, included in the label of the samples (Table 1), correspond to the amounts of nitrogen introduced during the synthesis. Samples containing nitrogen were washed three times in order to remove the excess of salts and therefore to eliminate the residual NH_4^+ and Cl^-. In fact, the NH_4^+ ions show an XPS peak at about 400 eV, the same binding energy as the N photoactive species in TiO_2/N.

The reasons for the enhancement of the photoactivity with N-doping are still not clear, regarding the chemical nature of doping centers and the modification of the band structure. Now authors mostly agree on the fact that the presence of N leads to a band gap narrowing, with an interband gap some tenths of electronvolts over the valence band. The nitrogen species can be incorporated to the TiO_2 lattice in a substitutional or interstitial position. In the substitutional position, a nitrogen atom substitutes an oxygen at a regular lattice site while in the interstitial position the nitrogen atom is chemically bound to a lattice oxygen. Substitutional N-doping can be excluded in our study, since the corresponding peak around 396-7 eV is never present. This is consistent with literature, where

the substitutional nitrogen is usually only observed for materials prepared by physical methods [56]. At this stage, even if interstitial N-doping is generally favored in sol-gel chemistry and consistent with the 400 eV peak [38], the decomposition of the N peak does not allow to claim the presence of Ti–O–N interstitial species only.

The highest photocatalytic activity is obtained for co-doped samples, assuming a combination of positive effects of both dopants.

The obtained photo-efficiency can be compared with literature. However, the large range of operating conditions reported in the photocatalytic experiments makes the comparison difficult. Indeed, the pollutant, its concentration, the illumination, or the catalyst amount were often different from one study to another.

In Gil et al. [54], sol-gel N-doped TiO_2 photocatalysts were synthesized and tested on the degradation of different emergent pollutants as caffeine, diclofenac, ibuprofen and salicylic acid. The photoactivity was evaluated under UV radiation with very low pollutant concentrations (1–15 ppm) and a catalyst concentration of 0.1 to 1 g/L. The degradation was faster than in our study, only 2 h, due to the higher energetic light used (UV radiation vs. visible light).

In Smirniotis et al. [53], N-doped TiO_2 is produced by a flame aerosol method to enhance visible activity. The degradation of phenol was conducted for 2 h and the comparison with commercial Evonik P25 was performed. The catalyst concentration was 1 g/L and the phenol concentration was 5×10^{-4} M. The best N-doped catalyst degraded 50% of phenol while P25 degraded only less than 5%. Our model pollutant, PNP, is a more complex molecule than phenol. The reaction time was therefore higher (24 h). However, when comparing our best sample with P25, the gain in photoactivity was similar to Smirniotis et al. [53].

In Suwannaruang et al. [57], Fe/N co-doped TiO_2 was synthesized via sol-gel hydrothermal method. The photoactivity was evaluated on the degradation of ciprofloxacin (20 mg/L corresponding to 6×10^{-5} M) under LED illumination (no information available about the wavelength) and a catalyst concentration of 1 g/L. The best catalyst (2.5 % N–1.5 % Fe) degraded 67% of ciprofloxacin after 6 h. Our best catalyst, TiO_2/Fe0.5/N43, degraded 67% of PNP after 24 h with a concentration of 10^{-4} M.

In Aba-Guevara et al. [49], Fe/N co-doped TiO_2 was also synthesized via sol-gel and microwave methods. The photoactivity was evaluated on the degradation of amoxicillin and streptomycin with a concentration of 30 mg/L ($\sim 8 \times 10^{-5}$ M and 5×10^{-5} M) under visible light (> 400 nm). The catalyst concentration was 1 g/L. After 5 h of illumination, the best sample (the sol-gel one with 0.7% Fe/0.5% N) degraded 42% of amoxicillin and 26% of streptomycin. A relevant comparison is difficult because those molecules are different from PNP.

A previous study of our laboratory reported the photoactivity obtained, in similar operating conditions, but with TiO_2/ZrO_2. When comparing the results, a better activity is reached with our TiO_2/Fe0.5/N43 sample than the TiO_2/ZrO_2 sample (67 vs. 40% of PNP degradation in same conditions [31]).

2.6. Film Crystallinity and Thickness

Films were deposited on three substrates with different colloids presented in the first part of this study: the TiO_2/Fe0.5 and the TiO_2/Fe0.5/N43 colloids. Coatings with pure TiO_2 were also made for comparative purposes.

The films were washed with water and dried before characterization to ensure the adhesion of the coating to the substrate. For all samples, the film remains unmodified after washing; the surface is slightly iridescent.

The crystallinity of the TiO_2 coatings was assessed using grazing incidence X-ray diffraction (GIXRD). Similar patterns were obtained for all samples; only the TiO_2/Fe0.25/N43 pattern deposited on brushed steel is represented in Figure 7. The broad peak at 25°, associated to anatase, is clearly observed. Regarding the peak shape, it is similar to the one obtained with the powder (Figure 1). Indeed, the broadness of the peak is caused by the very low value of the crystallite sizes (around 4 nm,

Table 1). Some additional peaks are observed around 32, 43 and 51° corresponding to the brushed stainless steel substrate (chromium oxide PDF 00-059-0308 and chromium PDF 01-088-2323 phases).

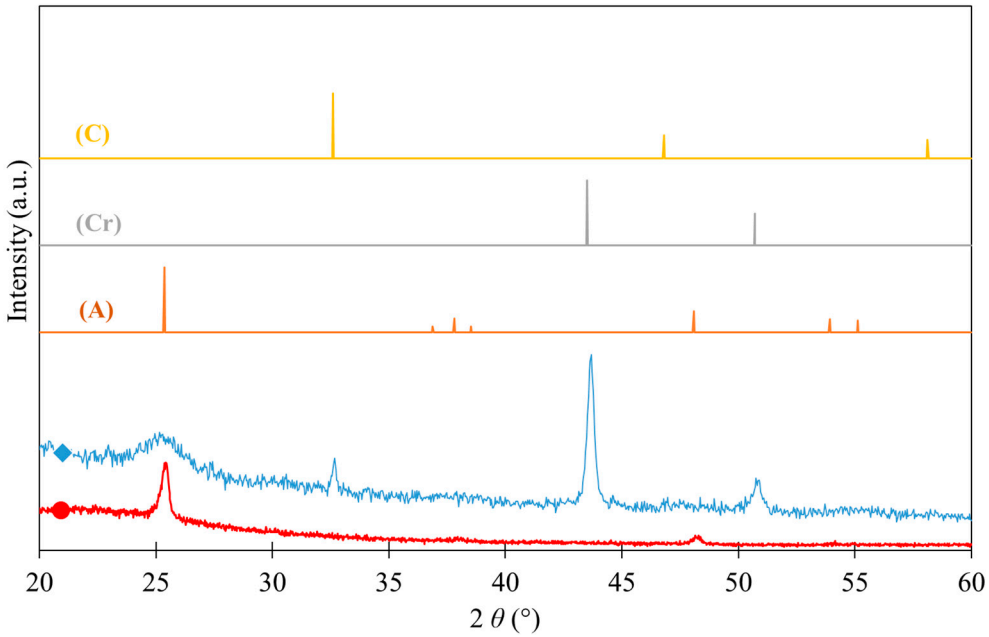

Figure 7. Grazing incidence X-ray diffraction (GIXRD) pattern of (♦) a TiO_2/Fe0.25/N43 film on steel, (●) a calcined TiO_2 film on glass, (A) reference pattern of anatase, (Cr) reference pattern of chromium, and (C) reference pattern of chromium oxide.

The presence of an additional layer between the substrate and the TiO_2 coatings was also investigated in order to point out the versatility of deposition. The GIXRD pattern of the calcined TiO_2 sublayer deposited on glass is presented in Figure 7. In this case, a highly crystalline TiO_2 sublayer was obtained.

Films produced by an aqueous sol-gel method typically have low thicknesses. As shown in a previous study [58], with the same deposition parameters, the thickness of a film deposited on a glass substrate is similar to the one obtained on steel for this type of sol-gel synthesis. The estimation gives a value of about 80 ± 10 nm on a glass substrate. Therefore, direct measurement of the thickness of the layer on steel is not possible by mechanical profilometry, since the roughness of the steel substrate is at the half-micron scale, or by optical profilometry, since the layer is transparent.

2.7. Photocatalytic Activity of the Films

The films were tested in two different setups in order to illustrate their photocatalytic potential in different situations. In the first case, a pesticide residue (PNP) was eliminated by the films under UV-A light. In the second case, LED light was used to degrade a dye (Rhodamine B).

The TiO_2/Fe0.5 colloid was deposited on different surfaces. The photoactivity was evaluated on PNP degradation. The results are presented in Table 3 after 72 h of illumination. A photocatalytic activity was maintained on each surface, highlighting its versatility of deposition. Generally, when a sublayer of anatase TiO_2 was present, the activity was increased due to this highly crystalline sublayer (Figure 7). Deposition on brushed steel gave higher PNP degradation than on bare steel. It can be assumed that the higher roughness of the brushed steel increased the surface of photocatalysts exposed to the light source. This substrate was therefore chosen for further PNP photocatalytic experiments with the optimized colloid composition identified in the first part of this study: the TiO_2/Fe0.5/N43 colloid (Section 2.5).

Table 3. PNP degradation (%) under UV-A light (λ = 365 nm) after 72 h for the TiO_2/Fe0.5 colloid deposited on various surfaces.

Sample	PNP Degradation after 72 h (%) ± 3
Brushed steel	26
Brushed steel + SiO_2 sublayer	19
Brushed steel + TiO_2 sublayer	32
Bare steel	18
Bare steel + SiO_2 sublayer	15
Bare steel + TiO_2 sublayer	12
Glass	26
Glass + TiO_2 sublayer	68

The photocatalysts are intended to be used for water depollution. Therefore, leaching experiments were performed with all samples from Table 3 in order to check the adherence of the films and the absence of TiO_2 or Fe leaching in water. The results are presented in Table S1, no leaching was detected whatever the sample.

Similar PNP degradation experiments were then performed with pure TiO_2 and TiO_2/Fe0.5/N43 coatings on brushed steel substrates. The evolution of the PNP degradation is presented in Figure 8.

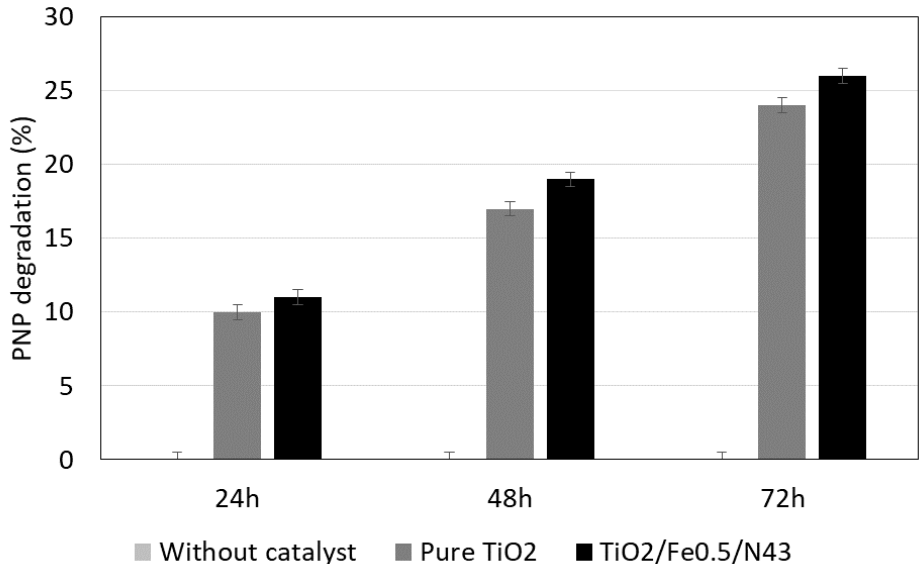

Figure 8. *p*-Nitrophenol (PNP) degradation (%) for pure TiO_2 and TiO_2/Fe0.5/N43 films under UV-A light (λ = 365 nm) after 24–48–72 h of illumination. No degradation took place without catalyst (error bars still shown).

The degradation of PNP increases with time (Figure 8). There is only a slight difference between pure TiO_2 and TiO_2/Fe0.5/N43 upon illumination at 365 nm. This is expected, since the desired effect of Fe- and N-doping is to shift the band gap energy to lower values. Thus, doped TiO_2 is barely at an advantage under UV-A light. Both photocatalysts are active at this wavelength as shown by Figure 4.

Nevertheless, when comparing absorbances (not shown here), values of 0.82 and 0.87 are obtained for pure TiO_2 and TiO_2/Fe0.5/N43 respectively with a ratio of 1.06 between the pure and the doped sample.

By contrast, while using LED light of wavelength 395 nm and RB, the degradation is much more significant for TiO_2/Fe0.5/N43 than for pure TiO_2. This difference in performance cannot be attributed to adsorption phenomena, which reach equilibrium after 20 min (not shown here). Figure 9 presents the variation of the concentration (normalized by the initial concentration) as a function of time.

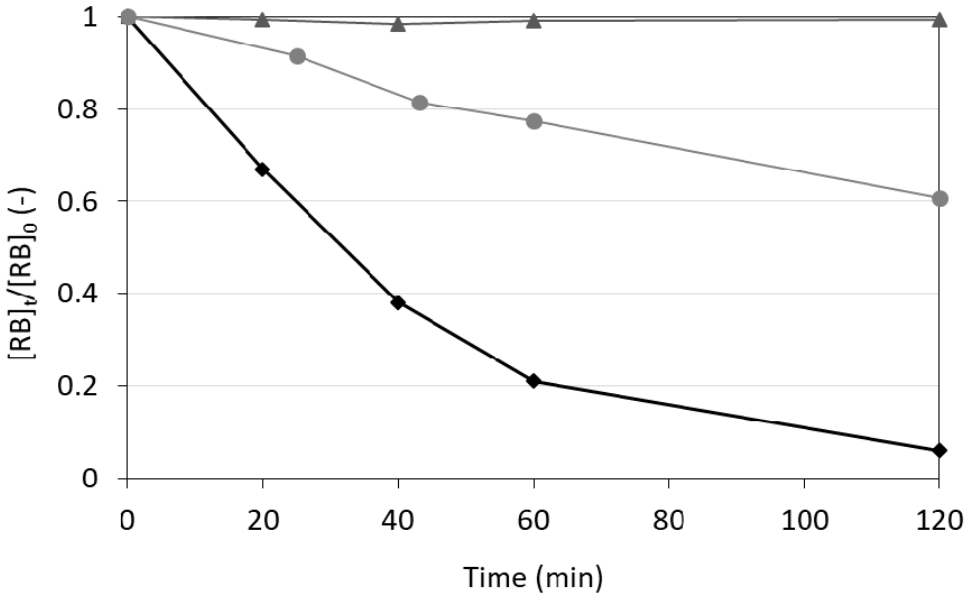

Figure 9. RB degradation for (●) pure TiO_2, (♦) TiO_2/Fe0.5/N43 films and (▲) without catalyst under LED light (λ = 395 nm) as a function of time.

Unlike in the previous case, RB can be sensitized by 395 nm light and contribute to its own degradation by interacting with TiO_2. This might explain the low, but nevertheless significant, degradation potential of pure TiO_2, alongside with the involuntary N-doping described in Section 2.4.

Upon this wavelength, pure TiO_2 has a low absorbance (0.59) and is less efficient than TiO_2/Fe0.5/N43 (0.79), with an absorbance ratio of 1.34 between the pure and the doped sample.

The longer the wavelength, the more efficient the degradation (energy-wise), since less energy is used for the creation of each e^--h^+ pair. Practically, it is particularly true when shifting from UV-A light to visible light, as visible LEDs are much more efficient than their UV-A counterparts. It confirms the assumption of the positive effect of the doping on the shift of the activity toward the visible region.

As reported in numerous papers, dye degradation usually follows a first-order reaction rate. An excellent fit of our data was obtained with the first-order rate equation:

$$-\mathrm{k}t = \ln\left(\frac{C}{C_0}\right) \tag{9}$$

where k is the rate constant, t is the time, and C and C_0 are the concentrations of pollutants at time t and initial time t_0, respectively. The kinetic constants were estimated using the least squares method (Table 4). As k depends on the number of active sites per unit volume of solution treated, a second rate constant k' can be calculated.

$$\mathrm{k}' = \mathrm{k}/\left(\frac{S}{V}\right) \tag{10}$$

where S is the surface of the photocatalyst and V is the volume of the solution. It is more representative of the efficiency of the photocatalyst.

Table 4. Kinetic rate constants of reactions with TiO_2 films.

	TiO_2/Fe0.5–PNP	TiO_2/Fe0.5/N43–RB
k (h^{-1})	6.52×10^{-3}	1.43
k' (h^{-1} $m^3_{solution}/m^2_{cata}$)	9.73×10^{-5}	2.13×10^{-2}
R^2 (correlation coefficient)	0.9996	0.9948

As mentioned earlier, a quantitative comparison to literature is hard to carry out. In this case, it would be limited to batch systems using photocatalytic films to degrade either pollutant, at similar

pH and not involving any additional chemical, as all these parameters influence the process. The observed kinetic constant k should be reported against the ratio *S*/*V* (otherwise, the constant ignores the amount of catalyst). Other parameters could be cited. Literature usually includes all information necessary to calculate the kinetic constant, but its value is rarely transferrable to other works.

In Lu et al. [59], kinetic constants range from 12.5×10^{-3} to 225×10^{-3} h^{-1} for PNP degradation, but the authors do not report the photocatalyst surface. In Kothavale et al. [60], a spray pyrolysis method is used in order to create N-doped TiO_2 films. In this case, the kinetic constant can be estimated to be around 0.168 h^{-1} for RB, but even though the area of the film is known, the total volume of solution is not. In Gastello et al. [61], TiO_2 films on $CoFe_2O_4$ particles are synthesized. The value of k' can be calculated and is around 6.9×10^{-2} h^{-1} $m^3_{solution}/m^2_{cata}$ for RB. The value is in the same order of magnitude, but higher. However, it must be noted that the authors use an optimal pH (3.5) and a powerful 500W-lamp.

2.8. Large-Scale Synthesis of TiO_2/Fe0.5

In order to point out a possible industrial production of our catalysts, the TiO_2/Fe0.5 material was produced at pilot scale in a 10 L glass reactor. This sample was chosen as it was a good compromise between enhanced activity under low energy light, compared to the pure sample, and the amount of dopant added. A picture of the 10 L colloid and the pilot reactor are presented in Figure S3 in the Supplementary Materials. This colloid was similar to the corresponding colloid obtained at laboratory scale, i.e., a blue-orange stable suspension.

The XRD pattern of the pilot scale TiO_2/Fe0.5 (Figure S4 in Supplementary Materials) is similar to the XRD pattern of the laboratory TiO_2/Fe0.5 (Figure 1) with the main peaks of anatase and a small fraction of brookite. The PNP degradation with the pilot scale TiO_2/Fe0.5 was 42% ± 3% after 8 h of illumination, which is similar to the degradation reached with the laboratory TiO_2/Fe0.5 (Figure 6). This comparison highlighted the efficient scale-up from laboratory to pilot scale, going one step further to a pre-industrial implementation.

3. Materials and Methods

3.1. Pure TiO_2 Synthesis

The undoped TiO_2 catalyst was prepared using titanium (IV) tetraisopropoxide (TTIP, >97%, Sigma-Aldrich, St. Louis, MO, USA), nitric acid (HNO_3, 65%, Merck, Suprapur, Fort Kennerworth, NJ, USA), isopropanol (IsoP, 99.5%, Acros Organics, Fisher Scientific, Hampton, NH, USA), and distilled water as starting materials.

First, 250 mL of distilled water was acidified with HNO_3 to reach a pH of 1. In a second vessel, 35 mL of TTIP was mixed with 15 mL of IsoP for 15 min. Then, the TTIP-IsoP mixture was added to the acidified water under stirring at 80 °C. After 24 h, a light blue sol was obtained [45]. Part of the sol was used directly to produce thin films on stainless steel. The remaining sol was dried under ambient air to obtain a white powder. The undoped TiO_2 sample is labelled pure TiO_2.

Evonik P25 TiO_2 material was used as reference material and is denoted P25.

3.2. Doped and Co-Doped TiO_2 Synthesis

Several Fe, N single-doped and co-doped TiO_2 catalysts were prepared. Two different Fe/Ti molar percentages were studied: 0.25 mol% and 0.5 mol% starting from ferric nitrate ($Fe(NO_3)_3 \cdot 9H_2O$, Merck). The N content varied between 10 and 75 mol% starting from ammonium chloride (NH_4Cl, UCB, Leuven, Belgium). The dopant(s) was (were) dissolved in the acidified water before addition to the TTIP-IsoP mixture. After 24 h, white to light blue stable sols were obtained. Samples were then dried under ambient air at room temperature. Samples containing nitrogen were washed three times with water to remove the excess of nitrogen salt. Finally, all samples were dried at 100 °C for 12 h. Prior to the drying, part of the sol was deposited on various substrates.

Samples are denoted as TiO_2/FeX/NY, with X and Y corresponding to the starting content (in mol%) of Fe and N respectively.

3.3. Film Deposition

Films were produced by bar-coating with an Elcometer 4340 Automatic Film Applicator (Elcometer Limited, Edge Lane, Manchester, UK) with a bar-speed of 1 cm s^{-1}. Films were coated on three substrates: bare and brushed stainless steel substrates (7.5 cm × 2.5 cm × 0.8 cm, 316L stainless steel, Mecanic Systems, Braine-l'Alleud, Belgium) and glass microscope slides (AF32ECO, Schott AG, Mainz, Germany). Films were dried at 100 °C for 30 s, washed with distilled water, dried with compressed air, and finally dried again at 100 °C for 30 s to get a perfectly clean surface and to remove non-adherent TiO_2 material.

Three suspensions were used for film application: pure TiO_2, TiO_2/Fe0.5 and TiO_2/Fe0.5/N43.

Films were also deposited on different sublayers to evaluate the versatility of deposition of the aqueous TiO_2 colloids. For bare and brush stainless steel substrates, two sublayers were tested: a sublayer of anatase TiO_2 synthesized as [29,41], calcined 1 h at 500 °C, and a sublayer of sol-gel SiO_2 synthesized according to [62]. For glass substrate, only anatase TiO_2 sublayer was evaluated.

3.4. Powder Characterization

The actual amount of iron in the doped TiO_2 samples was determined by inductively coupled plasma–optical emission spectroscopy (ICP–OES, Varian Inc., Palo Alto, CA, USA) with a Varian Liberty Series II. Solutions for analysis were prepared as follows: (i) 0.2 g of sample was digested in 12 mL of HCl (37%) + 6 mL of HNO_3 (65%) + 2 mL of HF (40%); (ii) the solution was then transferred into a 200 mL calibrated flask, finally filled with deionized water. The solution was then analyzed using the ICP-OES device.

Nitrogen adsorption–desorption isotherms were measured at 77K on a multi-sampler Micromeritics ASAP 2420 (Micromeritics, Norcross, GA, USA). Those isotherms provide information on the textural properties of the samples, such as the specific surface area, S_{BET}, by the Brunauer-Emmett- Teller (BET) method, the specific micropore volume, V_{DR}, by the Dubinin-Radushkevich theory and the pore volume, V_p, calculated from the adsorbed volume at saturation. Pore volume can be determined precisely enough for non-macroporous materials, which is the case in this study, except for P25.

An average particle size, d_{BET}, was estimated from S_{BET} values by assuming spherical and non-porous TiO_2 anatase nanoparticles using the following formula [33]:

$$\frac{d_{BET}}{6} = \frac{\frac{1}{\rho_{Anatase}}}{S_{BET}} \quad (11)$$

where $\rho_{Anatase}$ is the apparent density of TiO_2 anatase, estimated to be equal to 3.89×10^3 kg m^{-3} [20].

The crystallographic properties were determined using X-ray diffraction (XRD). The powder patterns were recorded with a Bruker D8 Twin-Twin powder diffractometer (Bruker, Billerica, MA, USA) using Cu-K_α radiation. The size of the TiO_2 crystallites, d_{XRD}, was determined via the Scherrer formula (Equation (12)):

$$d_{XRD} = 0.9\frac{\lambda}{(B\cos\theta)} \quad (12)$$

where d_{XRD} is the crystallite size (nm), B the peak full-width at half maximum after correction of the instrumental broadening (rad), λ the wavelength (nm), and θ the Bragg angle (rad).

The semi-quantitative analysis of phases was performed using the Profex software [63]. This program is based on Rietveld refinement method [64,65].

The samples were observed by transmission electron microscopy (TEM) with a Phillips CM 100 device with an accelerating voltage of 200 kV.

The optical properties were evaluated by diffuse reflectance in the 250–800 nm region with a Perkin Elmer Lambda 1050 S UV/VIS/NIR spectrophotometer, equipped with a spectralon coated integrating sphere (150 mm InGaAs Int. Sphere from PerkinElmer, Waltham, MA, USA) and using Al_2O_3 as reference. The absorbance spectra were transformed using the Kubelka–Munk function [33,66,67] to produce a signal, normalized for comparison between samples. The values of the band gaps ($E_{g,direct}$ and $E_{g,indirect}$) were estimated for all samples. The details of this method are widely described elsewhere [26,55].

X-ray photoelectron spectra were obtained with a SSI-X-probe (SSX-100/206) Fisons spectrometer (Surface Science Instruments, Mountain View, CA, USA) equipped with a monochromatized microfocused Al X-ray source (1486.6 eV), operating at 10 kV and 20 mA. The analysis chamber, in which samples were placed, was under a pressure of 10^{-6} Pa. Sample charging was adjusted using flood gun energy at 8 eV and a fine-meshed nickel grid placed 3 mm above the sample surface [68]. The pass energy was set to 150 eV and the spot size was 1.4 mm^2. The normal to the surface of the sample and the direction of electron collection formed an angle of 55°. Under these conditions, the mid-height width (FWHM) of the Au *4f7/2* peak photo-peak measured on a standard sample of clean gold was about 1.6 eV. The following sequence of spectra was recorded: survey spectrum, C *1s*, O *1s*, N *1s*, Fe *2p* and Ti *2p* and again C *1s* to check the stability of charge compensation with time and the stability of the samples over time.

The C–(C, H) component of the carbon C *1s* peak was set to 284.8 eV in order to calibrate the scale in binding energy. Three other components of the carbon peak (C–(O, N), C=O or O–C–O and O–C=O) were resolved, giving insight on how much oxygen was present because of carbon contamination. Data was processed by using the CasaXPS software (Casa Software Ltd, Teignmouth, UK). Some spectra were decomposed using the Gaussian and Lorentzian function product model (least squares fitting) after subtraction of a nonlinear Shirley baseline [69].

3.5. Film Characterization

The crystallinity of the films was characterized by grazing incidence X-ray diffraction (GIXRD) in a Bruker D8 diffractometer using Cu K_α radiation and operating at 40 kV and 40 mA. The incidence beam angle was 0.25°.

The film thickness was estimated by profilometry (Veeco Dektak 8 Stylus Profiler, Bruker, Billerica, MA, USA) on a film deposited on glass (Marienfeld Superior – 25 mm × 75 mm × 1 mm, Paul Marienfeld GmbH & Co. KG, Lauda-Königshofen, Germany) in the same deposition conditions as for steel.

Leaching experiments were performed with the coated substrates to evaluate their integrity in water. For each sample, the coated slide was placed in 50 mL of ultrapure water under stirring. After 48 h, the water was analyzed by ICP-OES to detect Ti and Fe. The detection limit was 0.03 and 0.01 ppm for Fe and Ti respectively.

3.6. Photocatalytic Activity of the Powders under Visible Light

The photocatalytic activity of all catalysts was determined through the degradation of a model pollutant, *p*-nitrophenol (PNP) for 24 h. The experimental set-up was described in a previous article [33,45]. For each catalyst, sealed batch reactors were exposed to a halogen lamp with a continuous spectrum from 300 to 800 nm (300 W, 220 V) measured with a Mini-Spectrometer TM-UV/vis C10082MD (Hamamatsu, Japan). A UV filter placed on the lamp eliminated wavelengths shorter than 400 nm. The temperature of the lamp and the reactors was maintained at 20 °C by a cooling system with recirculating water. The catalyst powder was dispersed in PNP solution ($C_0 = 10^{-4}$ kmol m^{-3}) in order to reach 1 kg m^{-3} in each batch reactor. A constant mixing was maintained by magnetic stirrers. Three reactors were used for each catalyst in order to study the reproducibility of the results. Furthermore, for each photocatalyst, dark tests (catalyst + PNP without light) were performed in order to take into account the potential adsorption of the pollutant onto the catalyst. One additional flask was exposed to light without catalyst to evaluate PNP natural decomposition under visible light.

No spontaneous break down of the PNP in the absence of catalyst was detected, so that any decrease of PNP concentration could be attributed to the catalytic degradation. The entire system was isolated in the dark in order to prevent interaction with the room lighting.

The degradation of PNP was determined by measuring the absorbance of PNP by UV/Vis spectroscopy (GENESYS 10S UV–Vis from Thermo Scientific, Waltham, MA, USA) at 317 nm. The degradation percentage of PNP, D_{PNP}, was calculated by Equation 13 for each batch reactor:

$$D_{PNP}(\%) = \left(1 - \frac{[PNP]_{24h}}{[PNP]_0}\right) \times 100\ \% \quad (13)$$

where $[PNP]_{24h}$ represents the residual concentration of PNP at time t = 24 h and $[PNP]_0$ represents the initial concentration of PNP at time t = 0 h.

3.7. Photocatalytic Activity of the Films

The photocatalytic activity of TiO_2 films was evaluated (i) by monitoring the degradation of *p*-nitrophenol (PNP) under ultraviolet light (UV-A, Osram Sylvania, Blacklight-Bleu Lamp, F 18W/BLB-T8, OSRAM GmbH, Munich, Germany) and (ii) by monitoring the degradation of rhodamine B (RB) under visible LED light (LED Würth Elektronic WL-SUMW SMT Ultraviolet Ceramic Waterclear, Würth Elektronik GmbH & Co. KG, Waldenburg, Germany) in two similar photocatalytic experiments.

The spectra of the lamps were measured with a Mini-Spectrometer TM-UV/vis C10082MD from Hamamatsu. UV-A and LED lights can be considered as quasi monochromatic with a wavelength of 365 nm and 395 nm respectively.

The experimental procedure is very similar for both pollutants. Indeed, each coated steel slide was placed in a Petri dish with 25 mL of PNP solution (10^{-4} kmol m^{-3}) or RB solution (2.5×10^{-6} kmol m^{-3}). The Petri dish was closed with a lid in order to avoid evaporation. The degradations of PNP or RB were evaluated from absorbance measurements with a Genesys 10S UV-Vis spectrophotometer (Thermo Scientific, Waltham, MA, USA) at 317 nm or 554 nm respectively. Adsorption tests were performed in the dark (dark tests) to determine whether PNP or RB was adsorbed by the films or the substrates. Blank tests, consisting of irradiating the pollutant solution in a Petri dish without any catalyst or support, were carried out to estimate the decomposition of PNP or RB under the corresponding light. The Petri dishes with catalyst and pollutant were stirred on orbital shakers at 80 rpm. Aliquots of PNP or RB were sampled along the experiment and put back in the Petri dishes after absorbance measurements to keep the volume constant. The photocatalytic degradation is equal to the total degradation of PNP or RB taking the catalyst adsorption (dark test) into account. Each photocatalytic measurement was triplicated to assess the reproducibility of data.

Regarding the PNP degradation, different substrates (bare steel, brushed steel and glass) and sublayers (TiO_2, SiO_2) were tested with the TiO_2/Fe0.5 coating. Then only pure TiO_2 and TiO_2/Fe0.5/N43 deposited on brushed stainless steel were evaluated through the degradation of PNP.

Regarding the RB degradation, only the coatings deposited on brushed steel without sublayer were evaluated, starting from pure TiO_2 and TiO_2/Fe0.5/N43 colloids.

3.8. Large-Scale Synthesis of TiO_2/Fe0.5

The large-scale synthesis was carried out in a 10 L pilot glass reactor (Figure S3 in Supplementary Materials) with a jacket warming system. First, 7.2 L of distilled water was acidified by HNO_3 to reach a pH of 1. Then, 1 L of TTIP was added to 300 mL of IsoP and 6.5 g of $Fe(NO_3)_3 \cdot 9H_2O$. The mixture was stirred at room temperature for 30 min. The mixture was then added to the acidified water and stirred at 250 rpm. The reaction took place for 4 h at 80°C. A blue-orange translucent sol was obtained, and a small fraction (50 mL) was dried under ambient air to obtain a powder.

The corresponding powder was analyzed by XRD (Section 3.4), and its photoactivity was evaluated on the degradation of PNP (Section 3.6).

4. Conclusions

In this work, an aqueous sol-gel process was successfully applied to produce Fe, N single-doped and co-doped TiO_2 photocatalysts at low temperature without any calcination step. Different *dopant/Ti* molar ratios were tested: 0.25 or 0.5 mol% of Fe and 10 to 75 mol% of N (starting concentrations). The corresponding undoped TiO_2 catalyst was synthesized for comparison.

The physico-chemical characterizations showed that catalysts are composed of nano-crystalline anatase-brookite particles, with higher specific surface areas than P25 (~ 200 $m^2\ g^{-1}$ vs. 47 $m^2\ g^{-1}$). All samples presented a higher visible absorption than P25. The XPS spectra showed that all the samples were doped with nitrogen, leading to a shift of the activity toward visible. Both dopants extend the TiO_2 photoactivity toward the visible region with the best result for a co-doped sample. The optimal starting composition is TiO_2 doped with 43 mol% of nitrogen and 0.5 mol% of iron.

Thin films were produced on stainless steel with the undoped TiO_2 and the best N-Fe co-doped sample. The photoactivity was estimated under 365 nm UV-A light and 395 nm visible LED light. The doped sample had a better activity than the pure one, with a clear enhancement under the longer wavelength (395 nm). This confirms the positive influence of the dopants on the shift of activity toward the visible region. The versatility of the photocatalysts was demonstrated on the degradation of two molecules, *p*-nitrophenol and rhodamine B, and on the deposition on different surfaces. A colloid synthesis was efficiently scaled-up from laboratory to 10 L pilot scale. Those results highlight the possibility of producing photocatalytic films without any calcination step and active under LED light, whose energy consumption is lowest in the visible range. This constitutes a step forward for an industrial development.

Supplementary Materials: The following are available online at http://www.mdpi.com/2073-4344/10/5/547/s1, Figure S1: Nitrogen adsorption–desorption isotherm of Evonik P25, Figure S2: XPS general spectrum of the pure TiO_2 sample, Figure S3: Large-scale suspension of TiO_2/Fe0.5 and the pilot reactor used for its synthesis, Figure S4: XRD patterns of the large-scale TiO_2/Fe0.5 sample. (A) Reference pattern of anatase and (B) Reference pattern of brookite, Table S1. Ti and Fe leaching for the TiO_2/Fe0.5 colloid deposited on various surfaces after 48 h in water.

Author Contributions: Conceptualization, methodology, writing, S.D.; investigation and analysis, S.D., J.G.M. and C.R.; writing–original draft preparation, S.D., J.M. and C.W.; DR-UV-Vis absorbance, D.P.; X-ray photoelectron spectroscopy, F.D. and E.M.G.; supervision, funding acquisition and project administration, S.D.L.; correction of the paper before submission: all authors. All authors have read and agreed to the published version of the manuscript.

Funding: Authors are grateful to the Département de la Recherche et du Développement technologique DGO6 of the Service Public de Wallonie and GreenWin, Competitivity Cluster of Wallonia, for financial support under Grant n°7744 (BlueV project).

Conflicts of Interest: The authors declare no conflict of interest. The funders had no role in the design of the study; in the collection, analyses, or interpretation of data; in the writing of the manuscript, or in the decision to publish the results.

References

1. Khan, M.A.; Ghouri, A.M. Environmental Pollution: Its Effects on Life and Its Remedies. *Res. World J. Arts Sci. Commer.* **2011**, *2*, 276–285.
2. Pignatello, J.J.; Oliveros, E.; MacKay, A. Advanced Oxidation Processes for Organic Contaminant Destruction Based on the Fenton Reaction and Related Chemistry. *Crit. Rev. Environ. Sci. Technol.* **2006**, *36*, 1–84. [CrossRef]
3. Kuyukina, M.S.; Ivshina, I.B. Application of Rhodococcus in Bioremediation of Contaminated Environments. In *Biology of Rhodococcus*; Springer: Berlin/Heidelberg, Germany, 2010; pp. 231–262. [CrossRef]
4. Mills, A.; Le Hunte, S. An overview of semiconductor photocatalysis. *J. Photochem. Photobiol. A Chem.* **1997**, *108*, 1–35. [CrossRef]
5. Di Paola, A.; García-López, E.; Marcì, G.; Palmisano, L. A survey of photocatalytic materials for environmental remediation. *J. Hazard. Mater.* **2012**, *211–212*, 3–29. [CrossRef] [PubMed]

6. Rauf, M.A.; Ashraf, S.S. Fundamental principles and application of heterogeneous photocatalytic degradation of dyes in solution. *Chem. Eng. J.* **2009**, *151*, 10–18. [CrossRef]
7. Fujishima, A.; Hashimoto, K.; Watanabe, T. *TiO_2 Photocatalysis: Fundamentals and Applications*; Bkc: Tokyo, Japan, 1999; ISBN 493905103X 9784939051036.
8. Hoffmann, M.R.; Martin, S.T.; Choi, W.; Bahnemann, D.W. Environmental Applications of Semiconductor Photocatalysis. *Chem. Rev.* **1995**, *95*, 69–96. [CrossRef]
9. Linsebigler, A.L.; Lu, G.; Yates, J.T. Photocatalysis on TiO_2 Surfaces: Principles, Mechanisms, and Selected Results. *Chem. Rev.* **1995**, *95*, 735–758. [CrossRef]
10. Pelaez, M.; Nolan, N.T.; Pillai, S.C.; Seery, M.K.; Falaras, P.; Kontos, A.G.; Dunlop, P.S.M.; Hamilton, J.W.J.; Byrne, J.A.; O'Shea, K.; et al. A review on the visible light active titanium dioxide photocatalysts for environmental applications. *Appl. Catal. B Environ.* **2012**, *125*, 331–349. [CrossRef]
11. Jo, W.-K.; Tayade, R.J. New Generation Energy-Efficient Light Source for Photocatalysis: LEDs for Environmental Applications. *Ind. Eng. Chem. Res.* **2014**, *53*, 2073–2084. [CrossRef]
12. Subagio, D.P.; Srinivasan, M.; Lim, M.; Lim, T.-T. Photocatalytic degradation of bisphenol-A by nitrogen-doped TiO_2 hollow sphere in a vis-LED photoreactor. *Appl. Catal. B Environ.* **2010**, *95*, 414–422. [CrossRef]
13. Oseghe, E.O.; Ofomaja, A.E. Study on light emission diode/carbon modified TiO_2 system for tetracycline hydrochloride degradation. *J. Photochem. Photobiol. A Chem.* **2018**, *360*, 242–248. [CrossRef]
14. Casado, C.; Timmers, R.; Sergejevs, A.; Clarke, C.T.; Allsopp, D.W.E.; Bowen, C.R.; van Grieken, R.; Marugán, J. Design and validation of a LED-based high intensity photocatalytic reactor for quantifying activity measurements. *Chem. Eng. J.* **2017**, *327*, 1043–1055. [CrossRef]
15. Hossaini, H.; Moussavi, G.; Farrokhi, M. Oxidation of diazinon in cns-ZnO/LED photocatalytic process: Catalyst preparation, photocatalytic examination, and toxicity bioassay of oxidation by-products. *Sep. Purif. Technol.* **2017**, *174*, 320–330. [CrossRef]
16. Chevremont, A.-C.; Farnet, A.-M.; Coulomb, B.; Boudenne, J.-L. Effect of coupled UV-A and UV-C LEDs on both microbiological and chemical pollution of urban wastewaters. *Sci. Total Environ.* **2012**, *426*, 304–310. [CrossRef]
17. Ghosh, J.P.; Langford, C.H.; Achari, G. Characterization of an LED Based Photoreactor to Degrade 4-Chlorophenol in an Aqueous Medium Using Coumarin (C-343) Sensitized TiO_2. *J. Phys. Chem. A* **2008**, *112*, 10310–10314. [CrossRef]
18. Takano, T.; Mino, T.; Sakai, J.; Noguchi, N.; Tsubaki, K.; Hirayama, H. Deep-ultraviolet light-emitting diodes with external quantum efficiency higher than 20% at 275 nm achieved by improving light-extraction efficiency. *Appl. Phys. Express* **2017**, *10*, 031002. [CrossRef]
19. Epifani, M.; Giannini, C.; Tapfer, L.; Vasanelli, L. Sol–Gel Synthesis and Characterization of Ag and Au Nanoparticles in SiO_2, TiO_2, and ZrO_2 Thin Films. *J. Am. Ceram. Soc.* **2000**, *83*, 2385–2393. [CrossRef]
20. Espino-Estévez, M.R.; Fernández-Rodríguez, C.; González-Díaz, O.M.; Araña, J.; Espinós, J.P.; Ortega-Méndez, J.A.; Doña-Rodríguez, J.M. Effect of TiO2–Pd and TiO_2–Ag on the photocatalytic oxidation of diclofenac, isoproturon and phenol. *Chem. Eng. J.* **2016**, *298*, 82–95. [CrossRef]
21. Vaiano, V.; Iervolino, G.; Sannino, D.; Murcia, J.J.; Hidalgo, M.C.; Ciambelli, P.; Navío, J.A. Photocatalytic removal of patent blue V dye on Au-TiO_2 and Pt-TiO_2 catalysts. *Appl. Catal. B Environ.* **2016**, *188*, 134–146. [CrossRef]
22. Ofiarska, A.; Pieczyńska, A.; Fiszka Borzyszkowska, A.; Stepnowski, P.; Siedlecka, E.M. Pt–TiO_2-assisted photocatalytic degradation of the cytostatic drugs ifosfamide and cyclophosphamide under artificial sunlight. *Chem. Eng. J.* **2016**, *285*, 417–427. [CrossRef]
23. Semlali, S.; Pigot, T.; Flahaut, D.; Allouche, J.; Lacombe, S.; Nicole, L. Mesoporous Pt-TiO_2 thin films: Photocatalytic efficiency under UV and visible light. *Appl. Catal. B Environ.* **2014**, *150–151*, 656–662. [CrossRef]
24. Di Paola, A.; Marcì, G.; Palmisano, L.; Schiavello, M.; Uosaki, K.; Ikeda, S.; Ohtani, B. Preparation of Polycrystalline TiO_2 Photocatalysts Impregnated with Various Transition Metal Ions: Characterization and Photocatalytic Activity for the Degradation of 4-Nitrophenol. *J. Phys. Chem. B* **2002**, *106*, 637–645. [CrossRef]
25. Rauf, M.A.; Meetani, M.A.; Hisaindee, S. An overview on the photocatalytic degradation of azo dyes in the presence of TiO_2 doped with selective transition metals. *Desalination* **2011**, *276*, 13–27. [CrossRef]

26. Malengreaux, C.M.; Pirard, S.L.; Léonard, G.; Mahy, J.G.; Herlitschke, M.; Klobes, B.; Hermann, R.; Heinrichs, B.; Bartlett, J.R. Study of the photocatalytic activity of Fe3+, Cr3+, La3+ and Eu3+ single-doped and co-doped TiO_2 catalysts produced by aqueous sol-gel processing. *J. Alloys Compd.* **2017**, *691*, 726–738. [CrossRef]
27. Carp, O.; Huisman, C.L.; Reller, A. Photoinduced reactivity of titanium dioxide. *Prog. Solid State Chem.* **2004**, *32*, 33–177. [CrossRef]
28. Litter, M.I. Heterogeneous photocatalysis: Transition metal ions in photocatalytic systems. *Appl. Catal. B Environ.* **1999**, *23*, 89–114. [CrossRef]
29. Léonard, G.L.-M.; Malengreaux, C.M.; Mélotte, Q.; Lambert, S.D.; Bruneel, E.; Van Driessche, I.; Heinrichs, B. Doped sol–gel films vs. powders TiO_2: On the positive effect induced by the presence of a substrate. *J. Environ. Chem. Eng.* **2016**, *4*, 449–459. [CrossRef]
30. Léonard, G.L.-M.; Pàez, C.A.; Ramírez, A.E.; Mahy, J.G.; Heinrichs, B. Interactions between Zn2+ or ZnO with TiO_2 to produce an efficient photocatalytic, superhydrophilic and aesthetic glass. *J. Photochem. Photobiol. A Chem.* **2018**, *350*, 32–43. [CrossRef]
31. Mahy, J.G.; Lambert, S.D.; Tilkin, R.G.; Wolfs, C.; Poelman, D.; Devred, F.; Gaigneaux, E.M.; Douven, S. Ambient temperature ZrO_2-doped TiO_2 crystalline photocatalysts: Highly efficient powders and films for water depollution. *Mater. Today Energy* **2019**, *13*, 312–322. [CrossRef]
32. Papadimitriou, V.C.; Stefanopoulos, V.G.; Romanias, M.N.; Papagiannakopoulos, P.; Sambani, K.; Tudose, V.; Kiriakidis, G. Determination of photo-catalytic activity of un-doped and Mn-doped TiO_2 anatase powders on acetaldehyde under UV and visible light. *Thin Solid Films* **2011**, *520*, 1195–1201. [CrossRef]
33. Malengreaux, C.M.; Douven, S.; Poelman, D.; Heinrichs, B.; Bartlett, J.R. An ambient temperature aqueous sol-gel processing of efficient nanocrystalline doped TiO_2-based photocatalysts for the degradation of organic pollutants. *J. Sol-Gel Sci. Technol.* **2014**, *71*, 557–570. [CrossRef]
34. Granados, G.; Martínez, F.; Páez-Mozo, E.A. Photocatalytic degradation of phenol on TiO_2 and TiO_2/Pt sensitized with metallophthalocyanines. *Catal. Today* **2005**, *107–108*, 589–594. [CrossRef]
35. Mahy, J.G.; Paez, C.A.; Carcel, C.; Bied, C.; Tatton, A.S.; Damblon, C.; Heinrichs, B.; Man, M.W.C.; Lambert, S.D. Porphyrin-based hybrid silica-titania as a visible-light photocatalyst. *J. Photochem. Photobiol. A Chem.* **2019**, *373*, 66–76. [CrossRef]
36. Tasseroul, L.; Pirard, S.L.; Lambert, S.D.; Páez, C.A.; Poelman, D.; Pirard, J.-P.; Heinrichs, B. Kinetic study of p-nitrophenol photodegradation with modified TiO_2 xerogels. *Chem. Eng. J.* **2012**, *191*, 441–450. [CrossRef]
37. Hu, L.; Wang, J.; Zhang, J.; Zhang, Q.; Liu, Z. An N-doped anatase/rutile TiO_2 hybrid from low-temperature direct nitridization: Enhanced photoactivity under UV-/visible-light. *RSC Adv.* **2014**, *4*, 420–427. [CrossRef]
38. Di Valentin, C.; Pacchioni, G.; Selloni, A.; Livraghi, S.; Giamello, E. Characterization of Paramagnetic Species in N-Doped TiO_2 Powders by EPR Spectroscopy and DFT Calculations. *J. Phys. Chem. B* **2005**, *109*, 11414–11419. [CrossRef]
39. Mahy, J.G.; Cerfontaine, V.; Poelman, D.; Devred, F.; Gaigneaux, E.M.; Heinrichs, B.; Lambert, S.D. Highly efficient low-temperature N-doped TiO_2 catalysts for visible light photocatalytic applications. *Materials (Basel)* **2018**, *11*, 584. [CrossRef]
40. Iwase, M.; Yamada, K.; Kurisaki, T.; Prieto-Mahaney, O.O.; Ohtani, B.; Wakita, H. Visible-light photocatalysis with phosphorus-doped titanium(IV) oxide particles prepared using a phosphide compound. *Appl. Catal. B Environ.* **2013**, *132–133*, 39–44. [CrossRef]
41. Bodson, C.J.; Heinrichs, B.; Tasseroul, L.; Bied, C.; Mahy, J.G.; Man, M.W.C.; Lambert, S.D. Efficient P- and Ag-doped titania for the photocatalytic degradation of waste water organic pollutants. *J. Alloys Compd.* **2016**, *682*, 144–153. [CrossRef]
42. Cheng, X.; Liu, H.; Chen, Q.; Li, J.; Wang, P. Construction of N, S codoped TiO_2 NCs decorated TiO_2 nano-tube array photoelectrode and its enhanced visible light photocatalytic mechanism. *Electrochim. Acta* **2013**, *103*, 134–142. [CrossRef]
43. Di Valentin, C.; Pacchioni, G. Trends in non-metal doping of anatase TiO_2: B, C, N and F. *Catal. Today* **2013**, *206*, 12–18. [CrossRef]
44. Lecloux, A. Exploitation des isothermes d'adsorption et de désorption d'azote pour l'étude de la texture des solides poreux. *Mém. Soc. R. Des Sci. Liège 6ème série* **1971**, *1*, 169–209.

45. Mahy, J.G.; Léonard, G.L.-M.; Pirard, S.; Wicky, D.; Daniel, A.; Archambeau, C.; Liquet, D.; Heinrichs, B. Aqueous sol–gel synthesis and film deposition methods for the large-scale manufacture of coated steel with self-cleaning properties. *J. Sol-Gel Sci. Technol.* **2017**, *81*, 27–35. [CrossRef]
46. Li, X.; Chen, Z.; Shi, Y.; Liu, Y. Preparation of N, Fe co-doped TiO_2 with visible light response. *Powder Technol.* **2011**, *207*, 165–169. [CrossRef]
47. Kim, T.-H.; Rodríguez-González, V.; Gyawali, G.; Cho, S.-H.; Sekino, T.; Lee, S.-W. Synthesis of solar light responsive Fe, N co-doped TiO_2 photocatalyst by sonochemical method. *Catal. Today* **2013**, *212*, 75–80. [CrossRef]
48. Su, Y.; Xiao, Y.; Li, Y.; Du, Y.; Zhang, Y. Preparation, photocatalytic performance and electronic structures of visible-light-driven Fe–N-codoped TiO_2 nanoparticles. *Mater. Chem. Phys.* **2011**, *126*, 761–768. [CrossRef]
49. Aba-Guevara, C.G.; Medina-Ramírez, I.E.; Hernández-Ramírez, A.; Jáuregui-Rincón, J.; Lozano-Álvarez, J.A.; Rodríguez-López, J.L. Comparison of two synthesis methods on the preparation of Fe, N-Co-doped TiO_2 materials for degradation of pharmaceutical compounds under visible light. *Ceram. Int.* **2017**, *43*, 5068–5079. [CrossRef]
50. Azouani, R.; Tieng, S.; Chhor, K.; Bocquet, J.-F.; Eloy, P.; Gaigneaux, E.M.; Klementiev, K.; Kanaev, A.V. TiO_2 doping by hydroxyurea at the nucleation stage: Towards a new photocatalyst in the visible spectral range. *Phys. Chem. Chem. Phys.* **2010**, *12*, 11325–11334. [CrossRef]
51. Bittencourt, C.; Rutar, M.; Umek, P.; Mrzel, A.; Vozel, K.; Arčon, D.; Henzler, K.; Krüger, P.; Guttmann, P. Molecular nitrogen in N-doped TiO_2 nanoribbons. *RSC Adv.* **2015**, *5*, 23350–23356. [CrossRef]
52. Livraghi, S.; Chierotti, M.R.; Giamello, E.; Magnacca, G.; Paganini, M.C.; Cappelletti, G.; Bianchi, C.L. Nitrogen-Doped Titanium Dioxide Active in Photocatalytic Reactions with Visible Light: A Multi-Technique Characterization of Differently Prepared Materials. *J. Phys. Chem. C* **2008**, *112*, 17244–17252. [CrossRef]
53. Smirniotis, P.G.; Boningari, T.; Damma, D.; Inturi, S.N.R. Single-step rapid aerosol synthesis of N-doped TiO_2 for enhanced visible light photocatalytic activity. *Catal. Commun.* **2018**, *113*, 1–5. [CrossRef]
54. Gil, A.; García, A.M.; Fernández, M.; Vicente, M.A.; González-Rodríguez, B.; Rives, V.; Korili, S.A. Effect of dopants on the structure of titanium oxide used as a photocatalyst for the removal of emergent contaminants. *J. Ind. Eng. Chem.* **2017**, *53*, 183–191. [CrossRef]
55. Mahy, J.G.; Lambert, S.D.; Léonard, G.L.-M.; Zubiaur, A.; Olu, P.-Y.; Mahmoud, A.; Boschini, F.; Heinrichs, B. Towards a large scale aqueous sol-gel synthesis of doped TiO_2: Study of various metallic dopings for the photocatalytic degradation of p-nitrophenol. *J. Photochem. Photobiol. A Chem.* **2016**, *329*, 189–202. [CrossRef]
56. El Koura, Z.; Cazzanelli, M.; Bazzanella, N.; Patel, N.; Fernandes, R.; Arnaoutakis, G.E.; Gakamsky, A.; Dick, A.; Quaranta, A.; Miotello, A. Synthesis and Characterization of Cu and N Codoped RF-Sputtered TiO_2 Films: Photoluminescence Dynamics of Charge Carriers Relevant for Water Splitting. *J. Phys. Chem. C* **2016**, *120*, 12042–12050. [CrossRef]
57. Suwannaruang, T.; Hildebrand, J.P.; Taffa, D.H.; Wark, M.; Kamonsuangkasem, K.; Chirawatkul, P.; Wantala, K. Visible light-induced degradation of antibiotic ciprofloxacin over Fe–N–TiO_2 mesoporous photocatalyst with anatase/rutile/brookite nanocrystal mixture. *J. Photochem. Photobiol. A Chem.* **2020**, *391*, 112371. [CrossRef]
58. Mahy, J.G.; Wolfs, C.; Mertes, A.; Vreuls, C.; Drot, S.; Smeets, S.; Dircks, S.; Boergers, A.; Tuerk, J.; Lambert, S.D. Advanced photocatalytic oxidation processes for micropollutant elimination from municipal and industrial water. *J. Environ. Manag.* **2019**, *250*, 109561. [CrossRef]
59. Lu, Y.; Xu, Y.; Wu, Q.; Yu, H.; Zhao, Y.; Qu, J.; Huo, M.; Yuan, X. Synthesis of Cu_2O nanocrystals/TiO_2 photonic crystal composite for efficient p-nitrophenol removal. *Colloids Surf. A Physicochem. Eng. Asp.* **2018**, *539*, 291–300. [CrossRef]
60. Kothavale, V.P.; Patil, T.S.; Patil, P.B.; Bhosale, C.H. Photoelectrocatalytic degradation of Rhodamine B using N doped TiO_2 thin Films. *Mater. Today Proc.* **2020**, *23*, 382–388. [CrossRef]
61. Gastello, E.; Estrada, D.; Estrada, W.; Luyo, C.; Espinoza, J.; Ponce, S.; de Oca, J.M.; Rodriguez, J.M. TiO_2 films on $CoFe_2O_4$ nanoparticles for the Photocatalytic oxidation of Rhodamine B: Influence of the alcoholic solutions. *Proc. SPIE* **2019**, *11371*, 113710C. [CrossRef]
62. Hao, S.; Lin, T.; Ning, S.; Qi, Y.; Deng, Z.; Wang, Y. Research on cracking of SiO_2 nanofilms prepared by the sol-gel method. *Mater. Sci. Semicond. Process.* **2019**, *91*, 181–187. [CrossRef]
63. Doebelin, N.; Kleeberg, R. Profex: A graphical user interface for the Rietveld refinement program BGMN. *J. Appl. Crystallogr.* **2015**, *48*, 1573–1580. [CrossRef] [PubMed]

64. Tobaldi, D.M.; Piccirillo, C.; Rozman, N.; Pullar, R.C.; Seabra, M.P.; Škapin, A.S.; Castro, P.M.L.; Labrincha, J.A. Effects of Cu, Zn and Cu-Zn addition on the microstructure and antibacterial and photocatalytic functional properties of Cu-Zn modified TiO_2 nano-heterostructures. *J. Photochem. Photobiol. A Chem.* **2016**, *330*, 44–54. [CrossRef]
65. Lopes, D.; Daniel-da-Silva, A.L.; Sarabando, A.R.; Arias-Serrano, B.I.; Rodríguez-Aguado, E.; Rodríguez-Castellón, E.; Trindade, T.; Frade, J.R.; Kovalevsky, A.V. Design of Multifunctional Titania-Based Photocatalysts by Controlled Redox Reactions. *Materials* **2020**, *13*, 758. [CrossRef] [PubMed]
66. Kubelka, P.; Munk, F. Ein Beitrag zur Optik der Farban striche. *Z. Tech. Phys.* **1931**, *12*, 593–601.
67. Kubelka, P. New contributions to the optics of intensely light-scattering materials. *J. Opt. Soc. Am.* **1948**, *38*, 448–457. [CrossRef]
68. Bryson, C.E. Surface potential control in XPS. *Surf. Sci.* **1987**, *189–190*, 50–58. [CrossRef]
69. Shirley, D.A. High-Resolution X-Ray Photoemission Spectrum of the Valence Bands of Gold. *Phys. Rev. B* **1972**, *5*, 4709–4714. [CrossRef]